JGR Solid Earth

RESEARCH ARTICLE
10.1029/2019JB019154

Concentrated Slip and Low Rupture Velocity for the May 20, 2012, M_W 5.8, Po Plain (Northern Italy) Earthquake Revealed From the Analysis of Source Time Functions

Vincenzo Convertito[1], **Nicola Alessandro Pino**[1], **and Davide Piccinini**[2]

[1]Istituto Nazionale di Geofisica e Vulcanologia, Osservatorio Vesuviano, Napoli, Italy, [2]Istituto Nazionale di Geofisica e Vulcanologia, Sezione di Pisa, Pisa, Italy

Key Points:

- We use a forward modeling and a Bayesian inverse method to image slip distribution of the May 20, 2012, M_W 5.8, Northern Italy, earthquake
- We found a bilateral rupture with concentrated slip
- We found slow rupture velocity

Correspondence to:
V. Convertito,
vincenzo.convertito@ingv.it

Citation:
Convertito, V., Pino, N. A., & Piccinini, D. (2021). Concentrated slip and low rupture velocity for the May 20, 2012, M_w 5.8, Po Plain (Northern Italy) earthquake revealed from the analysis of source time functions. *Journal of Geophysical Research: Solid Earth*, *126*, e2019JB019154. https://doi.org/10.1029/2019JB019154

Received 27 NOV 2019
Accepted 2 DEC 2020

Abstract We analyse the rupture properties of the May 20, 2012, M_W 5.8, Po Plain (Northern Italy) earthquake by using two different modeling procedures based on the source time functions: a forward modeling and a global inversion Bayesian method. While the forward modeling allows to retrieve general information on the source characteristics, the global inversion allows to explore a substantially larger number of possible solutions, with more parameters, providing a quantitative estimate of the misfit. We invert for the spatial slip distribution and for the rupture velocity on a planar fault model. The unknown slip is given at the nodes of the subfaults (control points) and then given at the elementary subfaults through a bilinear interpolation. The number of control points is progressively increased to move from a high- to low-wavelength description of final slip on the fault plane. The optimal model parameter set is chosen according to the Akaike Information Criterion. The uncertainty on the slip distribution and rupture velocity has been estimated by a statistical analysis of the model ensemble and, in particular, through the weighted mean model and the standard deviation.

We find that the most earthquake slip occurred in the regions located northeast and southwest of the hypocenter, consistent with the forward modeling. Moreover, we find a low rupture propagation velocity (0.4 compressional Mach number) similarly to what has been observed for the close 29 May, M_W 5.6, and radiation efficiency suggesting that half of the strain energy was used to create new fracture.

1. Introduction

The May 2012 seismic sequence occurred in the Po Plain (Northern Italy) and started on May 19, 2012, at 23:13:27 GMT with a M_L 4.1 (M_W 4.0) earthquake. On May 20 a M_L 5.9 (M_W 5.8) event was recorded, followed by a second M_L 5.8 (M_W 5.6) main shock on 29 May (http://cnt.rm.ingv.it/tdmt, Scognamiglio et al., 2006) and thousands of aftershocks, six of them with magnitude larger than 5.0 (Govoni et al., 2014) (Figure 1). The sequence took place on a south dipping blind thrust fault system (Ferrara arc) in the Emilia-Romagna region, covered by the quaternary sediment of the Po Plain. The largest events in the sequence are indeed characterized by reverse faulting style (e.g., Malagnini et al., 2012; Ventura & Di Giovambattista, 2013). Based on the Italian seismic classification the areas interested by the seismic sequence are classified as a low-to-moderate hazard (Stucchi et al., 2011). Indeed, expected peak-ground acceleration values with 10% probability of exceedance in 475 years range between 0.05 *g* and 0.25 *g* (being *g* the acceleration of gravity). However, the sequence caused 27 fatalities and widespread severe damage to dwellings forcing the closure of several factories (Lai et al., 2012). If on one hand part of the damage can be ascribed to site effects amplification (Castro et al., 2013) and to the performance of the industrial or civil structures (e.g., Liberatore et al., 2013; Manfredi et al., 2013; Masi et al., 2013), on the other hand it is important to understand the characteristics of the seismic source in order to assess its contribution to the general picture.

In spite of its impact, only a few analyses have been published on the source characteristics of the May 20 earthquake. The preliminary analyses of GPS (Serpelloni et al., 2012) and InSAR data (Bignami et al., 2012) only derived fault geometry by assuming uniform slip distribution. Successively, the analysis of the geodetic data (GPS and InSAR) by Pezzo et al. (2013) identified two main fault planes one

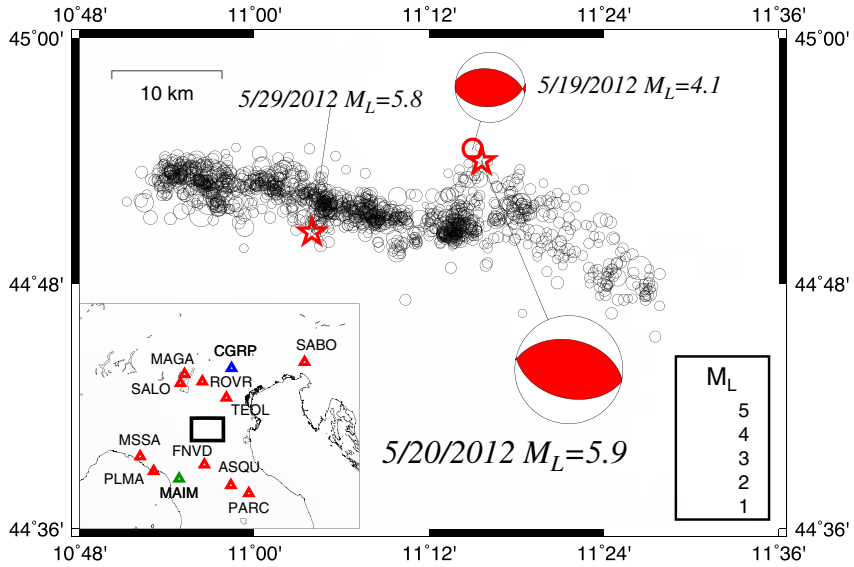

Figure 1. Geographic map showing the location of the May 20, M_L 5.9 (M_W 5.8), the May 29, M_L 5.8 (M_W 5.8), Po Plain (Northern Italy) earthquakes. The black circles, whose dimension is proportional to the magnitude, indicate the aftershocks occurred in the period May 20, 2012 to June, 2, 2012 and relocated by Govoni et al. (2014). The stations used in the present study belong to distinct networks and are indicated in the inset as triangles (red: Istituto Nazionale di Geofisica e Vulcanologia; blue: Istituto Nazionale di Oceanografia e Geofisica Sperimentale; green: Università di Genova). The location of the May 19, M_L 4.1 (M_W4.0), foreshock—used as empirical Greens' function in the present study—is also displayed with a red circle. The source mechanisms for the main event and for the empirical Greens' function are shown and correspond to the best double-couple of the TDMT solutions (http://cnt.rm.ingv.it/tdmt.html, Scognamiglio et al., 2006).

oriented N114° with a maximum slip of about 120 cm at 5 km depth and one oriented N95° with slip of about 30 cm between 3 and 7 km. The same study indicates that the following 29 May, M_W 5.6, event interested this latter plane. However, evidences for complex slip distribution was brought by Piccinini et al. (2012) who concluded that the rupture clearly features at least two distinct pulses separated by time intervals of about 1.5–2 s, with significant amount of energy radiated WSW. This complexity was imaged by Ganas et al. (2012), who inferred the distribution of slip, the rupture velocity, and the rise time of the event, using empirical Green's functions (EGFs) and a least squares inversion scheme of source time functions (STFs) computed from regional broadband seismological data. Conversely, Cesca et al. (2013), studying the directivity effect in the frequency domain 0.01–0.1 Hz, found that the rupture propagated unilaterally about 15 km toward SE. A similar rupture propagation direction was found by Convertito et al. (2013) as dominant direction, from the analysis of the peak-ground accelerations. The variability of the results obtained in the aforementioned analyses suggests that further investigations are required to better characterize the rupture history and the slip distribution. The aim of the present study is to analyse the rupture properties of the largest and most damaging event in the sequence, occurred on May 20. In particular, we analyse rupture kinematics and image the slip distribution from the analysis of the STFs—obtained by an empirical Green's functions approach—by using two different modeling procedures based on the source time functions: a forward modeling and a global inversion Bayesian method. The main advantage of using the STFs obtained by applying the EGFs technique is that uncertainties in structural as well as site effect model may be neglected. Indeed, as evidenced by Graves and Wald (2001), an inaccurate velocity structure could strongly bias the inverted slip distribution even when the rupture velocity, rise time, and rake angle are fixed. Moreover, the forward modeling allows to retrieve general information on the source characteristics, while the global inversion method implemented here allows to solve the nonlinear problem of inverting seismic data for the spatial slip distribution and rupture velocity on a fault.

2. Method

The source time function represents the temporal evolution of the seismic moment release during the propagation of the fracture and contains details about the history of the dislocation. Here we first applied a deconvolution technique to derive the relative source time functions for the 20 May, M_L 5.9, event and then derive information on the source kinematics by using forward and inverse modeling. The first approach allows to investigate the features of the STFs and to get a first rough picture of the rupture propagation (e.g., Convertito et al., 2016), while the inverse modeling leads to a more complete image of the slip pattern. Both approaches are based on the retrieval of the apparent moment rates radiated at different azimuths, by applying an empirical Green's function approach (see, for instance, Mori (2003) and reference therein). This technique consists of the deconvolution, at each station, of the seismograms relative to a suitable small event from the waveforms of the mainshock. If the hypocentral location and the source geometry of the two earthquakes are similar enough, the recording of the small event at a given station can be considered as EGF for that focal mechanism, i.e., representative of the structure response to an impulsive source characterized by the same fault geometry, for that specific source-receiver path. The results of the deconvolution represent the relative source time functions as seen at the relevant azimuth. The higher the corner frequency of the EGF and closer the small event to the mainshock, the higher the frequency resolution of the resulting relative STF (RSTF).

In principle, if the mainshock and the EGF have the same location and the same focal mechanism, their waveforms—filtered below the corner frequency of the large one, i.e., where both events can be considered as point source—have to be similar at each station. Thus, in order to search for the best EGF, we first chose a couple of test stations and estimated the corner frequency f_c of the mainshock at those sites, by using the method described by Snoke (1987). Then we performed a matched-filtered analysis, by sliding the waveforms of the mainshock along the continuous seismograms recorded at the same station throughout the period May 19 to June 8, with both signals previously low-pass-filtered below f_c. At each time step, we calculated the cross-correlation function, assuming that its maximum occurs at the time of the best EGF for the analyzed event. The results from this procedure have then been checked by visual inspection of the retrieved seismograms. The preferred EGF is the foreshock occurred on May 19, 2012, at 23:13:27 GMT with a M_L 4.1 (M_W 4.0) earthquake.

2.1. Forward Modeling

In the forward modeling we considered a simple pulse line source and tested different values for the kinematic source parameters, by comparing the predicted STFs with the observed ones. The approach is basically qualitative and aimed at retrieving basic information on the source characteristics that could also provide hints for interpreting the STFs, thus understanding what are their most stable and reliable features. This is particularly helpful when dealing with moderate magnitude events, whose source time functions are often affected by not negligible noise. Indeed, it has been successfully applied to the December 29, 2013, Matese, southern Italy, M_W 5.0, earthquake (Convertito et al., 2016).

In our approach, we started with a unilateral rupture and attempted at determining the parameters t, ϑ_d, and v_r providing a reasonably reproduction of the main features of the observed STFs. The result should give the main direction of propagation of the rupture and provide a first estimate of the source duration. Successively we explored the chance of bilateral rupture by adding a second line source propagating in a different direction and tested different shapes for moment rate by checking simple functions. When the main parameters are fixed, finally we tried to infer possible secondary features in the shape of the moment rate.

2.2. Bayesian Inversion Modeling

Here the direct problem is solved by computing slip at a set of control points (e.g., Emolo & Zollo, 2005) regularly distributed on the fault plane and then interpolating on a finer grid. To this aim we used a bilinear interpolation and filtered the slip map by using a Gaussian bi-dimensional filter (e.g., Király-Proag et al., 2019). The number of control points defines the size of the subfaults and is selected on the basis of the magnitude of the EGF. Indeed, the minimum size cannot be smaller than the estimated size of the EGF.

Each subfault is characterized by a single fault mechanism and described by three parameters: the final slip value, the rise time τ—defining the source time function—and the onset time. The size of the finer grid is selected according to the coherent rupture condition of six source points per wavelength (Archuleta & Hartzell, 1981). The method implemented in this study prescribes that the number of control points is progressively increased to move from a high-to-low wavelength description of final slip and rupture velocity on the fault plane (e.g., Emolo & Zollo, 2005). The optimal model parameter is finally chosen according to the minimum of the corrected Akaike Information Criterion parameter (Akaike, 1974). Nucleation point was located at the fault center and the rupture propagates at a constant rupture velocity. At each source depth we evaluated the v_P value (i.e., the propagation velocity of the selected seismic phase) using a specific crustal model for the area of interest and then computed the Mach number $\alpha = v_r/v_P$, being v_r the rupture velocity. Each subfault was allowed to slip only once with a triangular slip-rate function whose activation time from the origin time depends on the distance from the nucleation point, while the apparent activation time also depends on the source position with respect to the specific receiver according to the directivity function C_d. For a fault plane, the C_d function (Ben-Menahem, 1961) is:

$$C_d = \frac{1}{\left(1 - \alpha \cos \vartheta_{ri}\right)} \tag{1}$$

where α is the Mach-number and $\cos\vartheta_{ri}$ is given by

$$\cos \vartheta_{ri} = \cos\left(\varphi_r - \varphi_i\right)\sin \zeta_r \sin \zeta_i + \cos \zeta_r \cos \zeta_i \tag{2}$$

where ϑ_{ri} is the angle between the body wave radiated to station i (at azimuth φ_i and vertical takeoff angle ζ_i) and the rupture direction at azimuth φ_r and rupture angle ζ_r from vertically down. For each station the vertical takeoff angle ζ_i was computed by using the crustal model proposed for the area by Govoni et al. (2014). Although the EGF approach should allow to theoretically eliminate the effect of the propagation medium from the signal of the mainshock the use of the directivity function makes it necessary to introduce a velocity model in order to compute the take-off angle.

As for the inverse problem, we implemented the Metropolis-Hastings sampler approach (Metropolis et al., 1953) to investigate the model space parameter. Since for a given model $\mathbf{m}$ the next candidate point is generated as $\mathbf{m}_t = \mathbf{m}_{t-1} + \mathbf{z}$ where $\mathbf{z}$ is an increment random variable from a proposal distribution f, the approach corresponds to the random-walk Metropolis. The components of $\mathbf{m}$ are the rupture velocity v_r, the rise-time τ, and the slip distribution at a given number of points (control points). The best model parameter corresponds to the model that maximize the posterior distribution of the model space parameters, which is given by

$$f\left(\boldsymbol{m} \mid \boldsymbol{d}\right) = \frac{f\left(\boldsymbol{d} \mid \boldsymbol{m}\right)\rho\left(\boldsymbol{m}\right)}{\int_\Omega f\left(\boldsymbol{d} \mid \boldsymbol{m}\right)\rho\left(\boldsymbol{m}\right)d\boldsymbol{m}} \tag{3}$$

where $\mathbf{d}$ is the data vector and $\mathbf{m}$ is the model vector selected in the model space Ω, $\rho(\mathrm{m})$ is the priori distribution and $f(\boldsymbol{d}|\boldsymbol{m})$ is the likelihood function given by

$$f\left(\mathbf{d} \mid \mathbf{m}\right) = ce^{-Misfit} \tag{4}$$

and

$$Misfit = \frac{\sum_{i=1}^{Nstaz}\sum_{j=1}^{Nt}\left(S_{ij}^{cal} - S_{ij}^{obs}\right)^2}{\sum_{i=1}^{Nstaz}\sum_{j=1}^{Nt} S_{ij}^{obs\,2}} \tag{5}$$

In Equation 4, c is a normalization constant while in Equation 5, N_{staz} is the number of available stations and N_t is number of points of the source time functions S_i. As for the models' selection, after a given burn-in period, that is, a given number of iterations (e.g., the first 1,000 or so) (Gelman et al., 2004), a candidate model $\boldsymbol{m}_i$ is accepted if $f(\boldsymbol{d}|\boldsymbol{m}_i) > f(\boldsymbol{d}|\boldsymbol{m}_{i-1})$, otherwise it is accepted if the acceptance ratio $f(\boldsymbol{d}|\boldsymbol{m}_i)/f(\boldsymbol{d}|\boldsymbol{m}_{i-1})$ is

larger than η, where η is a number ranging between 0 and 1, randomly extracted from an uniform distribution. The advantage of using the ratio of the $f(\boldsymbol{d}|\boldsymbol{m}_i)$ functions is that it allows to avoid the computation of the normalization constant in equation (4) and to neglect the prior distribution thus reducing the problem of finding the maximum of the posterior distribution $f(\boldsymbol{m}|\boldsymbol{d})$ to minimizing the misfit function reported in Equation 5. At each iteration, the candidate models are obtained by using as proposal distribution a uniform distribution for both the rupture velocity and the rise-time, and the slip value at each control point. Similar to what has been done by Liu et al. (2006), we run the procedure 30 times starting from a different seed each time. From the analysis of the misfit of each model we identified the model with the lowest misfit and used the first 15 models to calculate the ensemble properties (e.g., Piatanesi et al., 2007). In particular, we considered the weighted average of slip maps using the misfit as weight, and the map of standard deviations. While the first allows the identification of the coherent features of the models, the standard deviation map allows us to estimate the uncertainty on the slip values in the different portions of the fault.

Next, starting from the slip map we computed a static stress drop map (Guatteri et al., 2004; Mai & Beroza, 2002). To this aim we used the relation between slip and stress proposed by Andrews (1980):

$$\Delta\sigma\left(\boldsymbol{k}\right) = -K\left(\boldsymbol{k}\right)\cdot D\left(\boldsymbol{k}\right) \tag{6}$$

where $\Delta\sigma(\boldsymbol{k})$ denotes the 2D transform in the wavenumber domain of the stress drop function and $D(\boldsymbol{k})$ the transform of the slip function. $K(\boldsymbol{k})$ represents the static stiffness function that for crustal rocks can be approximated as:

$$K\left(\boldsymbol{k}\right) = -\frac{1}{2}\mu k \tag{7}$$

where μ is the shear modulus (assumed as $3.3{\cdot}10^{10}$ Pa) and $k = \sqrt{k_x^2 + k_y^2}$ (Andrews, 1980). By using the stress drop distribution and the approach proposed by Guatteri et al. (2004), we computed the distribution of fracture energy G_C, that is, the amount of energy required to make the crack surface advance per unit surface (e.g., Lancieri et al., 2012; Rivera & Kanamori, 2005). In particular, Guatteri et al. (2004) provide an empirical relationship to compute G_C, once the stress drop map has been computed, that for event with magnitude lower than 6.5, is given by:

$$E\left(G_c \mid \boldsymbol{\beta}, \Delta\sigma, L_h\right) = 0.18 + 0.0015\Delta\sigma L_h^{1/2} \tag{8}$$

where $E\left(G_c \mid \boldsymbol{\beta}, \Delta\sigma, L_h\right)$ indicates the expected value of G_C, $\boldsymbol{\beta}$ is the vector containing the intercept and slope of the linear relation, $\Delta\sigma$ is the static stress drop, and L_h is the crack length computed as the distance of each point on the fault from the nucleation point as defined by Guatteri et al. (2004).

3. Results

We deconvolved the waveforms of the relevant EGF from those of the mainshock by spectral ratio with watering level correction, restricting the computation to the *P*-wave train. We selected broadband stations (all sampled at 100 Hz) within 250 km from the epicenter and used the vertical components. For each station, we performed several deconvolutions by slightly changing the P-wave train duration and verified that it did not affect the final STFs, giving stable results. Thus, we finally derived apparent moment rates at 12 stations and low-pass filtered the results at 1 Hz (Figure 2), well below the corner frequency of the EGF (3 Hz). We remark that at all the selected stations the signal-to-noise ratio (corresponding to the ratio between the mean amplitude of 10 s signal before and 10 s after the P-wave of the EGF) is higher than 20 (e.g., Figure 2).

The available sites are fairly well distributed with respect to the epicenter, with azimuthal gaps of 93° and 80° on the west and on the east side, respectively (inset in Figure 1). We note that, although the selected EGF is the best among the available aftershocks (according to the match filtering analysis), the resulting STFs still may be affected by the effect of small differences on the hypocentral location and focal mechanism between the mainshock and the selected aftershock.

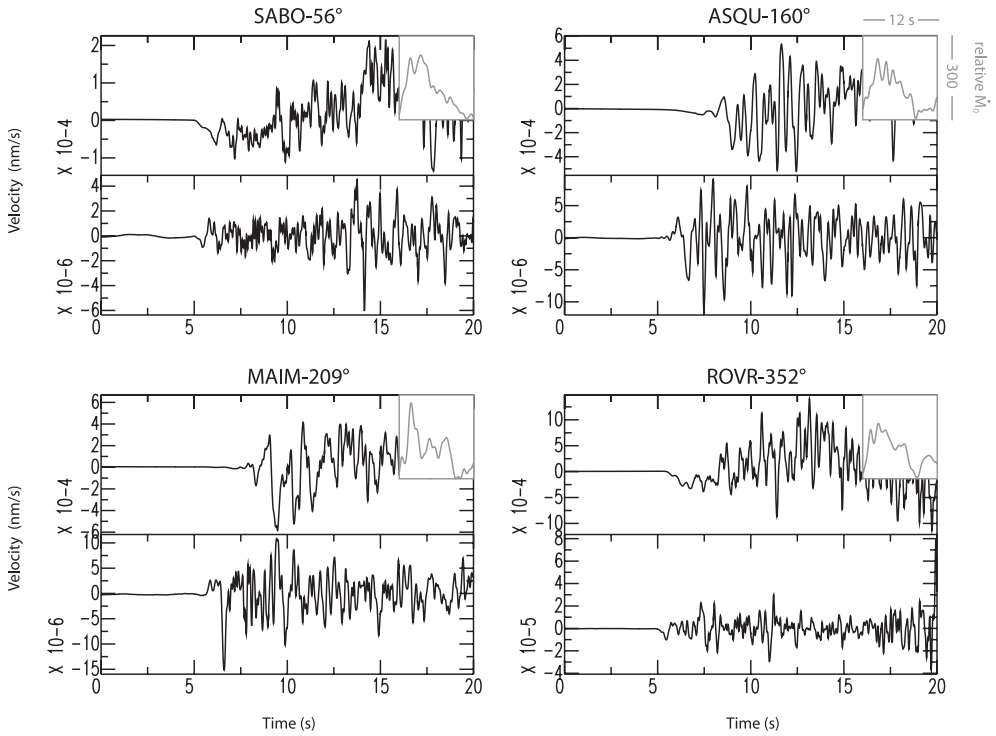

Figure 2. Examples of waveforms for the main shock (top trace) and the EGF (bottom trace). The STFs obtained from the deconvolution is shown in the inset. Each panel shows station codes, as indicated in Figure 1, along with the azimuth of the receiver relative to the source epicenter.

3.1. Forward Modeling

Overall, the relative STFs (RSTFs) display quite distinct waveforms at the various azimuths, with the largest amplitudes and frequencies at stations located South-West of the epicenter—between N200° and N230°—where a sharp pulse is well visible, while clearly smoother functions result to the N-NE. The breakage of symmetry indicates that some directivity effect is present and the features remarked aforementioned point to possible preferential rupture propagation toward the SW quadrant. However, both the duration and the maximum amplitude of the RSTFs do not change dramatically with azimuth. Incidentally, we notice that the total apparent duration is always larger than 7 s, with the minimum at PARC (source-to-station azimuth N149°), indicating that the actual total rupture cannot last less than that. If simple unilateral breakage occurred, RSTFs with significantly longer duration and lower amplitude should have resulted on one side. Instead, the lowest maximum amplitudes are indeed displayed at the stations located N-NW of the source, but these are not associated with the longest durations. These observations suggest a complex pattern of rupture propagation.

In order to obtain indications on the source kinematics, we performed a direct modeling of the retrieved moment rates. We first focused on matching the most energetic peak of the observed STFs. Thus, we started by assuming a unilateral rupture source with simple Gaussian moment rate and, by testing different rupture velocity values, we changed source duration and amplitude at the various azimuths according to the directivity equation $t_a = L\left(1 / v_r - \cos\vartheta / v_p\right)$, with t_a, L, and v_r, respectively, indicating the apparent duration, the rupture length, and the rupture velocity; while ϑ is the angle between the source-to-station direction and the rupture direction and v_p the P wave velocity in the source area. As for the rupture velocity, we tested a few values in the range 2.0–2.4 km/s that, however, given the complexity of the observed STFs and the simplistic assumed linear model, did not allow to discriminate a reliable best value. Thus we decided to use the average 2.2 km/s value. Based on the above observations, we used a source propagating toward the SW quadrant ($\vartheta_d = 225°$), with rupture duration $t_a = 7$ s, and rupture velocity $v_r = 2.2$ km/s—resulting in $L = 15.4$ km—and $v_P = 5.5$ km/s (Figure 3). The distinct durations and amplitudes displayed by the resulting

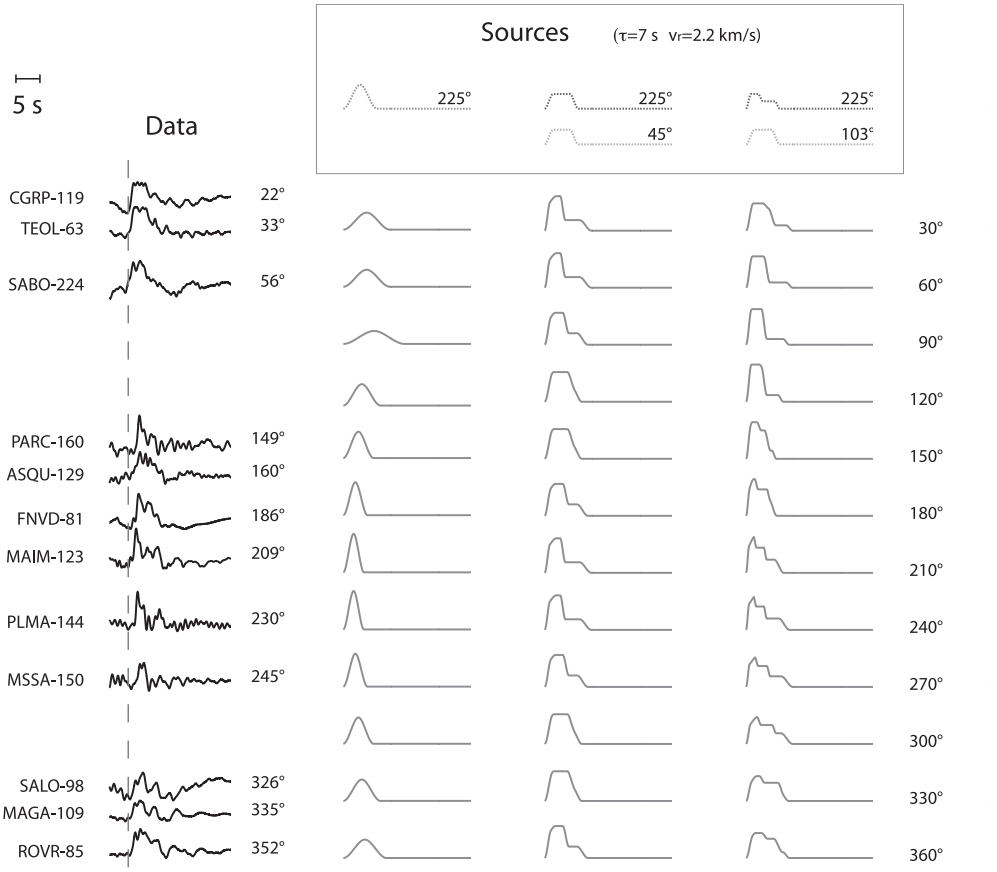

Figure 3. Black: STFs obtained by the deconvolution of the selected EGF. The vertical dashed line marks the time $t = 0$. The stations code, the epicentral distance in km, and the source-to-receiver azimuth are also reported. Gray: apparent moment rates predicted at fixed azimuths (indicated on the right). Each column displays the synthetic apparent STFs for the moment rate functions reported on the top of it, in the inset. All the ruptures are assumed to last 7 s and propagate at 2.2 km/s toward the azimuth indicated on each assumed source function.

functions indicate that, for the assumed source parameters, the apparent durations and amplitudes can be considered appropriate to give indications on possible preferential rupture directions. Moreover, the variation of the synthetic moment rate function with azimuth indicates that angle differences around 30° can be resolved. As for the actual source, the simple unilateral rupture accounts for the shape (frequency) of the main pulse present in the data. However, the model rupture predicts too low amplitude at opposite azimuth, where apparently considerable energy was actually propagated. Besides, the actual waveforms at the SW stations display some later energy that appears to be shorter at stations in the SE quadrant and rapidly smearing at other azimuths. These evidences imply that the source of the May 20 event must have released a significant seismic moment amount SW of the epicenter, but also that the rupture corresponds to a more complex rupture than a simple unilateral fracture.

Thus, we started with the assumption of purely symmetric bilateral fracture, with two equal subevents propagating toward opposite directions, and simply added a second source with 7 s duration as well, but propagating toward N45°. We used trapezoidal moment rate functions, more similar to the pulses observed in the data. It should be noticed that, at this level, we were interested at getting general information on the source directivity and not focused yet on the determination of realistic rupture lengths. The predicted RSTFs (Figure 3) display similar amplitude at all azimuth, similar to what observed in the data, supporting the hypothesis of multiple rupture propagating in definitely distinct—possibly opposite—directions. In addition to this basic consideration, the comparison addresses a few more points. The main pulse of the N225° source must be significantly shorter that what assumed. But, also, moving clockwise from N300° to

N60° the total duration of the actual RSTFs increases, indicating that, at those stations, the final part of the moment rate is to be due to SW propagating source. These two observations imply that the N225° propagating rupture do lasts about 7 s, like the model pulse; but it also has to be asymmetric, with a major sharp pulse in the first few seconds. On the other hand, moving clockwise from N300°, the initial ramp in the data becomes higher and steeper, meaning that this energy must be associated to a rupture propagated approximately eastward. Although the synthetic RSTFs well reproduce this feature, the N45° propagation azimuth also predicts a much faster variation than what observed, suggesting that this second rupture patch should have propagated at a larger angle from N. For what noted earlier, the two subevents must be superimposed in time.

Starting from these observations, we made a further test (Figure 3), with the N225° source shaped as described above, while for the second rupture we used a larger propagation angle. Based on the focal mechanism of the May 20, 2012 (INGV-TDMT catalog at http://cnt.rm.ingv.it/tdmt.html, Scognamiglio et al., 2006) and on the depth distribution of the aftershocks (Govoni et al., 2014), which indicate that the fault plane associated with the earthquake has strike directed to N103° and dip angle of 46°, as a tentative value we assumed N103° for the second rupture direction. The results are very satisfactory, with the major features—evidenced earlier—well reproduced. In particular, the model sources predict the observed distribution of both relative duration and amplitude, also producing the very similar moment rates observed northwest of the epicenter, the higher frequency observed to southern sites, and smoother apparent source time functions at the other stations.

Overall, the total durations appear to be correct. This means that, if larger rupture velocities v_r are imposed, the length L should also increase, reaching very large values (larger than 23 km) for a $M_W = 5.8$ earthquake (e.g., Wells & Coppersmith, 1994). Similarly, reducing L, the rupture velocity would be too low (lower than 1.55 km/s). For these reasons, we consider that adequate rupture parameters can be considered within ±30% of the adopted values. As for the P wave velocity in the source area v_P, it affects the results only to a very small extent: a 10% difference of v_P would result in 2% maximum variations of both duration and amplitude of the synthetic moment rate functions.

By considering the focal mechanism, our solution would correspond to a first subevent rupturing obliquely about 15 km downdip (the hypocentral depth is z < 7 km (Govoni et al., 2014)), followed by a second fracture directed approximately eastward, parallel to the fault strike and approximately 15 km long as well. In our modeling test, the two subevents are associated with a similar amount of seismic moment, 45% and 55% of the total $M_0 = 7.00359\ 10 + 17$ Nm, respectively, for the N225° and the N103° rupture directions. In order to get an estimate of the peak slip for the two rupture patches—which cannot be directly deduced by the observed STFs—we independently considered the two source time function deduced from the forward modeling and applied the modified Haskell source model used by Kanamori et al. (1992) to determine the slip distribution of the 1990 Landers earthquake. In particular, by stretching the moment rate to match the rupture length, it can be divided by the rupture velocity to give the seismic moment per unit length $m(l) = \mu w d$, where μ is the rigidity, w the rupture width, and d the slip. Therefore, dividing $m(l)$ by μw theoretical slip distributions along the rupture patches result. Albeit this scheme represents a crude approximation, it already proved to be effective in a number of cases, for both recent and historical seismic event (e.g., Pino et al., 1999; Pino et al., 2008), always giving results consistent with the geodetic and independent seismological analyses, when available. This model assumes unilateral fault propagation, thus we considered each subevent as a separate source and converted the moment rate into slip distribution along the direction of propagation of that specific fracture. As we assumed very simple moment rate functions, rather than imaging the slip distribution we were interested in getting hints about the maximum slip location and amplitude for the two rupture patches. For $\mu = 3 \times 10^{10}$ N/m^2 and $w = 3$ km, we got maximum slip of 0.53 m for both subevents; the first located approximately between 3 km and 6 km from the hypocenter moving downdip and southwest, the second eastward of the epicenter, along the fault plane.

3.2. Inverse Modeling

The STFs measured as reported in the previous sections are resampled at 0.05 s before implementing the inversion approach. We used a fault plane with length 26 km, width 12 km, and fault mechanism strike 103°, dip 46°, and rake 92° as given by TDMT (INGV-TDMT catalog at http://cnt.rm.ingv.it/tdmt.html,

Scognamiglio et al., 2006) corresponding to a reverse fault. The location of the fault center used as reference point, is at latitude 44.858 and longitude 11.298, at depth of 1 km corresponding to the top of the fault, while the nucleation point is located at 0 km along the strike and 7 km downdip. The dimension of the elementary faults is 0.06×0.06 km^2. The rupture velocity is explored in the range 1.6–3.6 km/s with steps of 0.1 km/s, while we set the rise-time at 0.4 s. The latter is selected by using the relationship between rise-time and M_0 provided by Somerville et al. (1999). The a priori slip distribution to be used in Equation 3 is selected as uniform, while the slip at each control point is perturbed by extracting random values in the range 0.0–0.7 m. The final slip maps are tapered on the border of the fault to avoid unrealistic stopping phases and the total radiated seismic moment is checked against the actual one by allowing a discrepancy of 25%.

We tested different number of control point configurations moving from high-to low-wavelength. For each control point configuration, we run 10 distinct procedures each exploring 10,000 models. Next, we computed the average model, which is used as starting model for the subsequent control point configurations. We use the Akaike Information Criterion (AIC) (Akaike, 1974) to select the best configuration. In particular, we searched for the minimum of the parameter AIC $= 2\mathrm{Np} + N[\ln(2\pi\hat{L}) + 1]$, where N is number of data (the product of number of STF samples and the number of STFs), Np is the number of parameters for each configuration, and $\hat{L}$ is the corresponding misfit value. For the investigated configurations we obtained: 3×2 ($\hat{L} = 0.01050$), 4×3 ($\hat{L} = 0.01114$), 5×4 ($\hat{L} = 0.01108$), 6×5 ($\hat{L} = 0.01030$), 7×6 ($\hat{L} = 0.01154$), 8×7 ($\hat{L} = 0.01079$), and 9×8 ($\hat{L} = 0.01198$). The test indicates that, excluding the configuration 3×2 that corresponds to a very high wavelength configuration, the model with 8×7 points along the strike and along the dip, respectively, provides the optimal compromise between model simplicity and adherence to data (Akaike, 1974). As reported in the Method section we run the procedure, consisting of 10,000 iterations, 30 times starting from a different seed each time. We identified as best model the one with the lowest misfit among the 30 results. Then we used the first 15 models identified according to their misfit value to calculate the ensemble properties (e.g., Piatanesi et al., 2007). In particular, for both the slip distribution and the rupture velocity, we computed the weighted mean model (where the weight is the inverse of the misfit value) and the standard deviation.

The best slip distribution is shown in Figure 4 indicating that the maximum slip value is 0.6 m and featuring at least two dominant directions. The first is along the strike of the fault while the second is toward southeast in agreement with the results of the direct approach obtained in this study. Remarkably, our slip distribution is in very good agreement with independent results obtained from the geodetic data obtained by Pezzo et al. (2013). On the other hand, Cesca et al. (2013) found a unilateral rupture direction, oriented toward SE. This difference is mainly due to the fact that Cesca et al. (2013) analyzed a lower frequency range (0.01–0.1 Hz), which, for this earthquake, allowed them to search only for the best unilateral rupture direction. However, we note that their rupture direction corresponds to the vector sum of the two dominant rupture directions found in our study.

Above the hypocenter and its surrounding region, the fault has slipped with amplitude 30% lower than that of two main patches. We note that these minor patches are not present in the geodetic solutions and thus are likely of limited extent and associated with high-frequency radiation. Consequently, they could not be resolved by the forward modeling.

The fit between the observed and synthetic STFs corresponding to the best model are shown in Figure 5 in the time domain and in Figure 6 in the frequency domain. Given the complexity of the observed STFs and the large areas not covered by the seismic stations in the suitable distance range the fit is quite satisfactory since it indicates that all the stations have a correlation coefficient larger than 0.7. The mean slip map and the map of the associated standard deviation are shown in Figure 7. We observe that the mean slip map suggests that the principal characteristics of the best model depicted in Figure 4a are a coherent feature of almost all the results obtained from the 15 selected lower misfit models. Moreover, the standard deviation map indicates that the largest part of the best slip map is well revolved. When evaluating the fit quality, it should be taken into account that part of the inconsistencies may be due to the fact that some stations are located close to the nodal planes of both the main event and the EGF, thus small differences can affect the retrieved EGF (see for instance PARC and ASQU located at similar azimuth but displaying significantly distinct STF). Moreover, we have assumed a planar fault and constant rupture velocity, which might be sim-

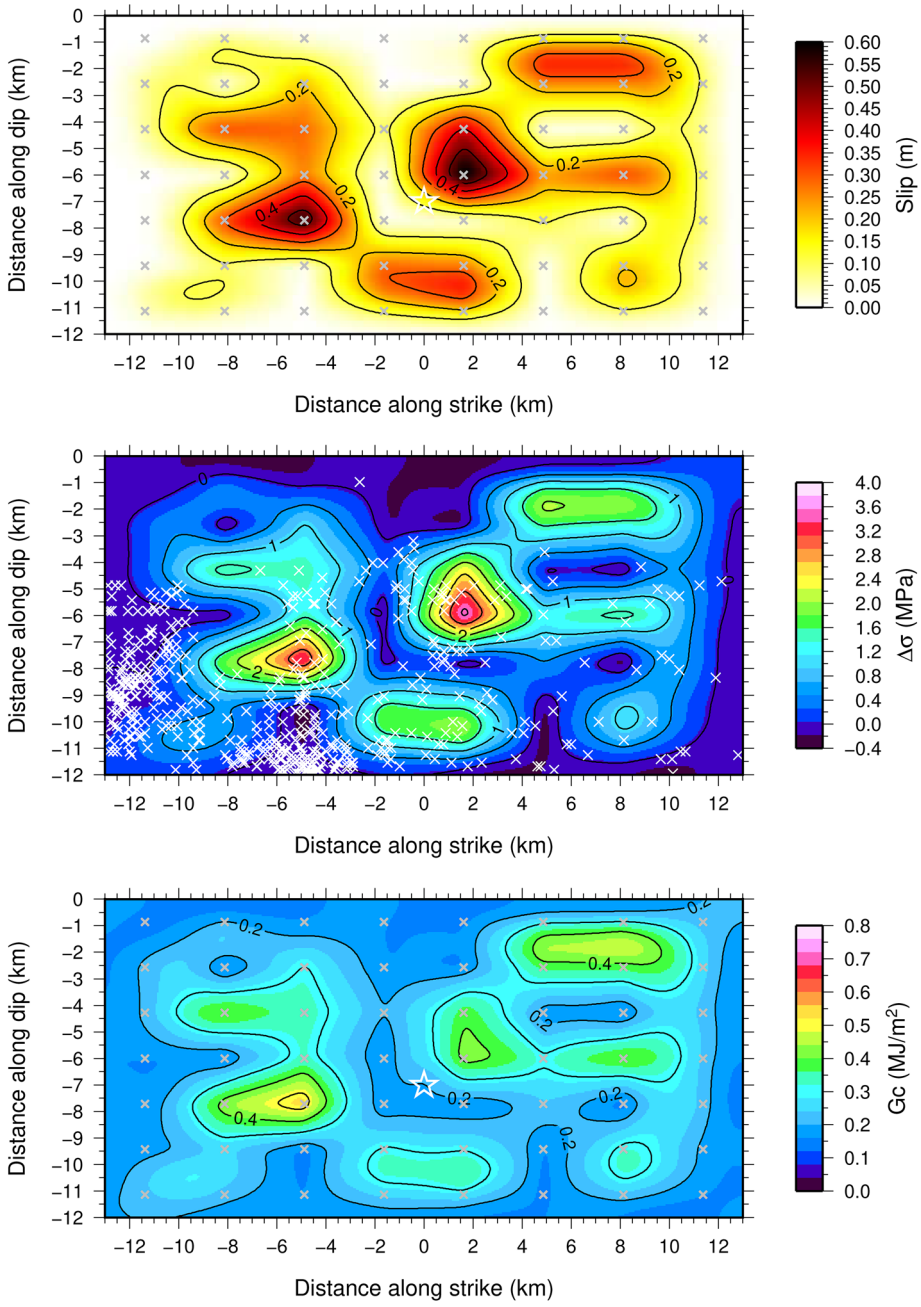

Figure 4. (a) Final slip map for the May 20, M_W 5.8, Po Plain (Northern Italy) earthquake corresponding to the synthetic STFs shown in Figure 5. The gray crosses identify the location of the control points while the white star represents the nucleation point position. (b) Static stress drop map obtained from the slip map distribution. White crosses correspond to the aftershocks relocated by Govoni et al. (2014). (c) Fracture energy computed by using the approach of Guatteri et al. (2004).

plistic assumptions for earthquakes occurring in a geological context as complex as the Po Plain-Northern Apennines region (e.g., Tondi et al., 2019).

The best velocity rupture value is 1.7 ± 0.2 km/s. Considering that the slip occurred in Jurassic limestones and upper Triassic carbonates (Bonini et al., 2014), and assuming the crustal model proposed by Govoni et al. (2014)—which indicates $v_P \geq 5.7$ km/s for these layers—the inferred rupture velocity value provides a relatively low compressional Mach number of 0.3 (corresponding to a shear wave Mach number of 0.5). A

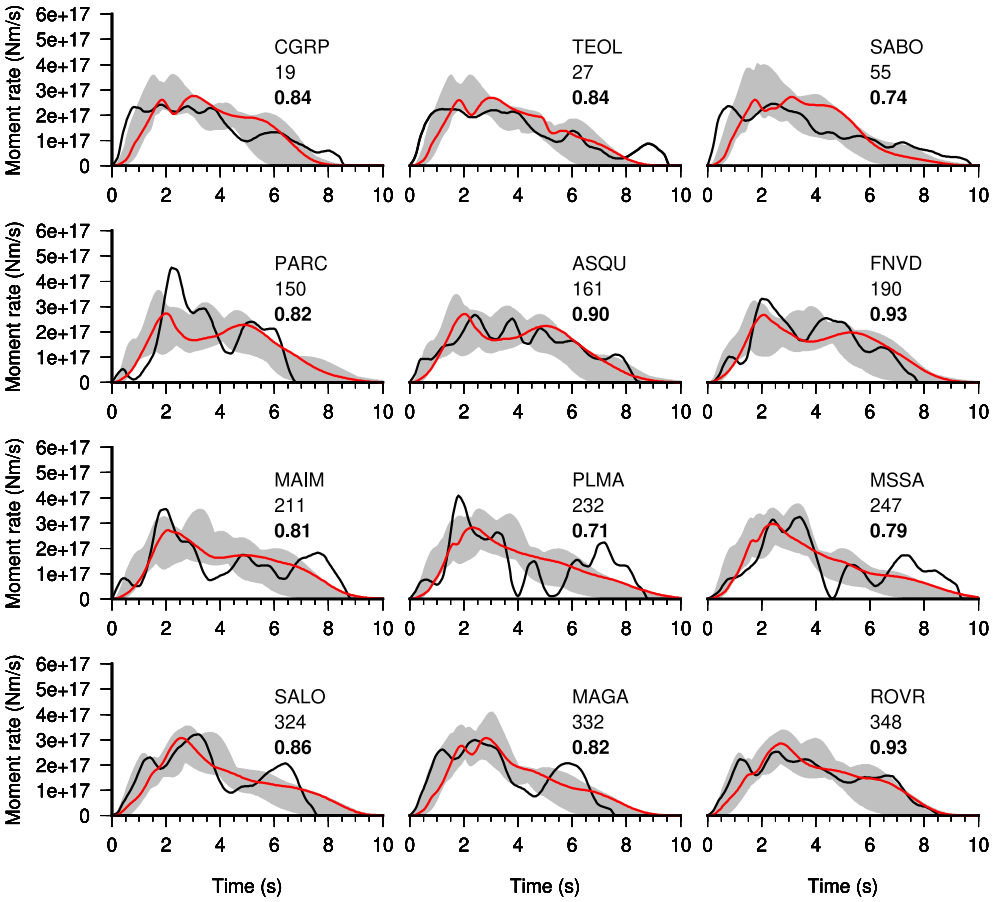

Figure 5. Observed source time functions (black lines) and synthetic (red lines) source time functions corresponding to the best solution obtained from the Bayesian inverse approach. The gray bands correspond to the STFs obtained from the model used to compute the mean slip map shown in Figure 7. In each panel the station code, the source-to-station azimuth, and correlation coefficient (bold) are reported.

similar slow rupture velocity has been observed also for the close 29 May, M_W 5.6, event (Causse et al., 2017) and interpreted as the fact that the fault was hard to break and that the fault strength was high in comparison to the initial stress level.

Finally, the map of the static stress drop (see Method section) is shown in Figure 4b along with the aftershocks recorded in the first month after the mainshock (Govoni et al., 2014) and projected on the fault plane. The result indicates a maximum stress drop of about 3.6 MPa, which is in agreement with the value of 2.9 MPa obtained by Castro et al. (2013) from the analysis of the S-wave spectral amplitude decay and that, as expected, the aftershocks occur around the main patches.

In order to strengthen this interpretation, we computed the apparent stress and the radiation efficiency from the analysis of the S-wave spectra. We first analyzed acceleration spectra at all the 26 available stations (Figure 8). However, due to the signal-to-noise ratio we obtained stable spectra at only eight stations (Table 1). Following Castro et al. (2013), we corrected the observed spectral amplitude for the near surface attenuation (Anderson & Hough, 1984) using $K_0 = 0.03$ and used the Q frequency dependent function for the anelastic attenuation $Q(f) = 80f^{1.2}$ proposed by Castro et al. (2013) for the area under study. Next, assuming a ω^{-2} spectrum (Brune, 1970) we fit the observed spectra—through a grid search approach—in order to estimate seismic moment (M_0), corner frequency (f_c), static stress ($\Delta\sigma = 0.44\, M_0/r^3$), and seismic energy. Static stress drop has been computed using the Brune's (1970) model for the corner frequency versus circular rupture radius relationship ($r = 0.37v_S/f_c$, being v_S the S-wave velocity, assumed 2.44 kms^{-1} as indicated by Castro

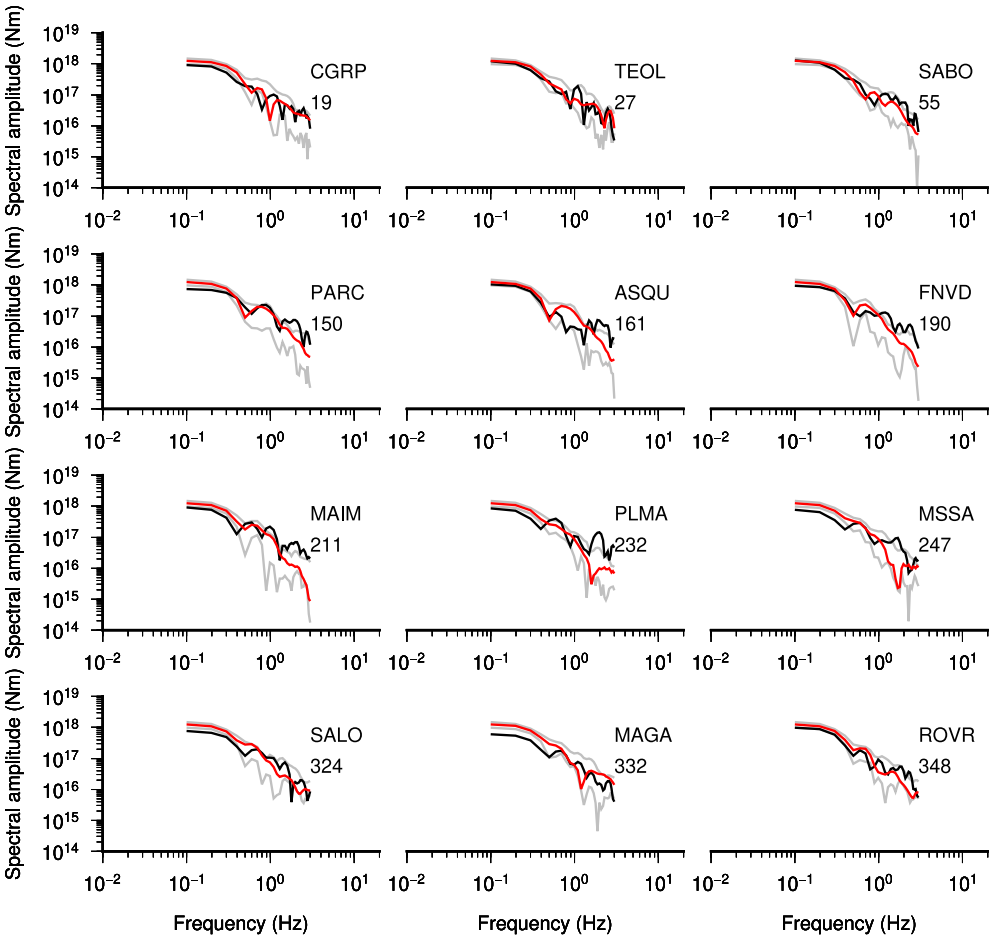

Figure 6. Spectra of the observed (black lines) and synthetic (red lines) source time functions corresponding to the best solution obtained from the Bayesian inverse approach. The gray curves correspond to the minimum and maximum at each frequency of the STFs obtained from the model used to compute the mean slip map shown in Figure 7. In each panel the station code, the source-to-station azimuth, are reported.

et al., 2013). Seismic energy is measured from the integral of squared ground motion velocity computed in the frequency domain, *Ic* (Boatwright & Fletcher, 1984):

$$E_s = \frac{4\pi\rho c R^2}{F^2} I_c = \frac{4\pi\rho c R^2}{F^2} \frac{1}{\pi} \int_0^\infty \omega^2 \mid U(\omega) \mid^2 d\omega \tag{9}$$

where R is the hypocentral distance, ρ the density, c the S-wave velocity and F the free surface coefficient. In eq. (9) I_c is measured in $(m/s)^2$ and E_s is expressed in Joule. As proposed by Zollo et al. (2014) we computed the displacement spectrum $U(\omega)$ from the best-fitting spectral model corrected for the frequency band limitation (e.g., Ide & Beroza, 2001). Seismic energy is then used to compute the apparent stress $\tau_a = \mu E_s / M_0$ (Wyss, 1979) with μ, the crustal shear modulus, set to $3.3 \cdot 10^{10}$ Pa. We obtained $f_c = 0.16$ Hz (0.11, 0.22), $\Delta\sigma = 2.9$ MPa (0.9, 8.7), $\tau_a = 1.2$ MPa (0.4, 3.4), $E_s = 6.7$ E + 13 J (5.9 E + 12, 9.8 E + 14). The uncertainties, which correspond to the 95% confidence intervals, have been computed by using the technique proposed by Prieto et al. (2007). The inferred value of corner frequency and static stress drop are in agreement with the values obtained by Castro et al. (2013). Using the apparent stress drop and the static stress drop we computed the radiation efficiency as $\eta_{SW} = \tau_a / \Delta\sigma$ providing 0.41.

In order to obtain a model independent estimate of η_{SW} we neglected the heat energy and computed the ratio between the radiated energy E_s and the total energy $E_S + E_G$, where E_G is total fracture energy. We used the stress drop map and the slip map inferred from the inverse modeling to compute the fracture energy

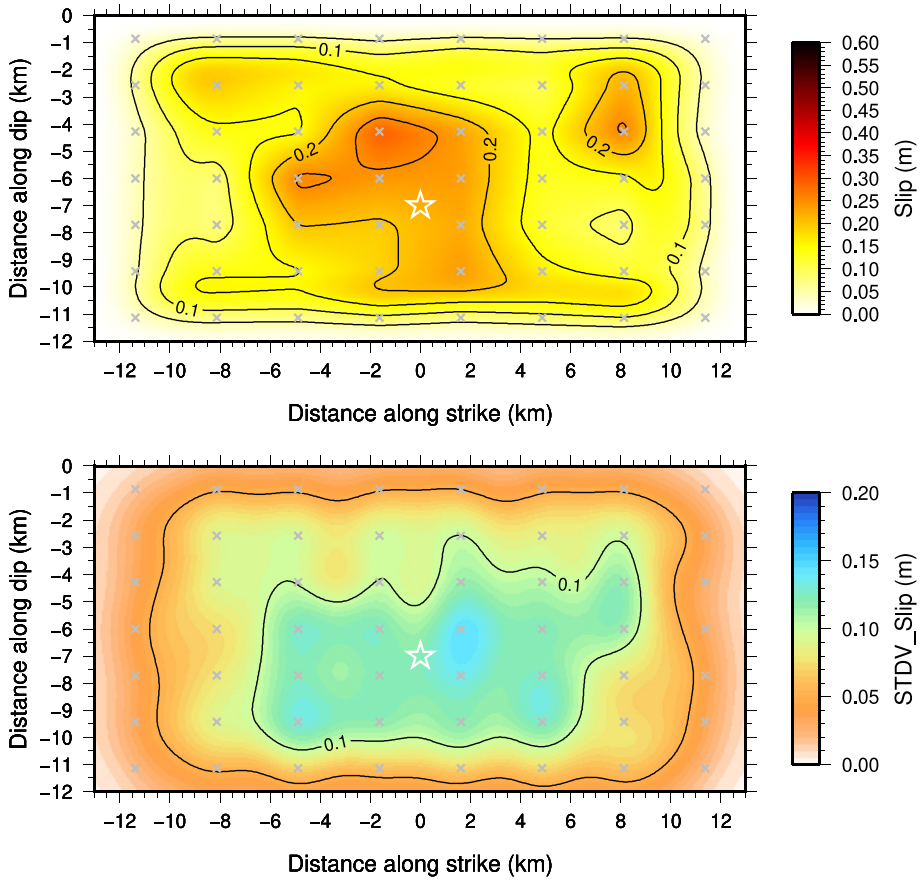

Figure 7. Average model (panel a) and standard deviation model (panel b) from ensemble inference.

density G_C map (Figure 4c). The result indicates a correlation between slip, stress drop and fracture energy with the highest value of G_C spent for fracturing the three main patches and, in particular, the downdip one. Thus, from G_C we computed E_G over the fault area, obtaining E_G = 7.6 10+13 J, which leads to a radiation efficiency of 0.47, confirming the estimate obtained by using the Brune model. This result indicates that more than half of the available energy was spent to propagate the rupture.

4. Conclusion

We have investigated the kinematic of the May 20, 2012, M_W 5.8, Po Plain (Northern Italy) earthquake from the analysis of the source time functions measured at 12 stations. In particular, we image the final slip map and the rupture velocity. To this aim we have implemented a twofold approach. The first is a forward modeling that was applied to investigate the rupture characteristics of the December 29, 2013, Matese, southern Italy, M_W 5.0, earthquake. The second approach is a multiscale Bayesian nonlinear inverse approach.

The two approaches provide consistent results, helping in defining the most robust features of the asperity breaking during the May 20, 2012, M_W 5.8, Po Plain (Northern Italy) earthquake. The whole picture suggests that the rupture was bilateral, characterized by two main slip patches of about 0.6 m, with a significant downdip component. These findings are in accordance with the results obtained by Pezzo et al. (2013) from the analysis of geodetic data.

The rupture propagation velocity resulted in 1.7 km/s, which is notably low and in line with the value found by Causse et al. (2017) for the close May 29, M_W 5.6, event. By estimating apparent stress and static stress drop from S-wave spectral amplitudes, we derived a radiation efficiency of 0.41, which corresponds

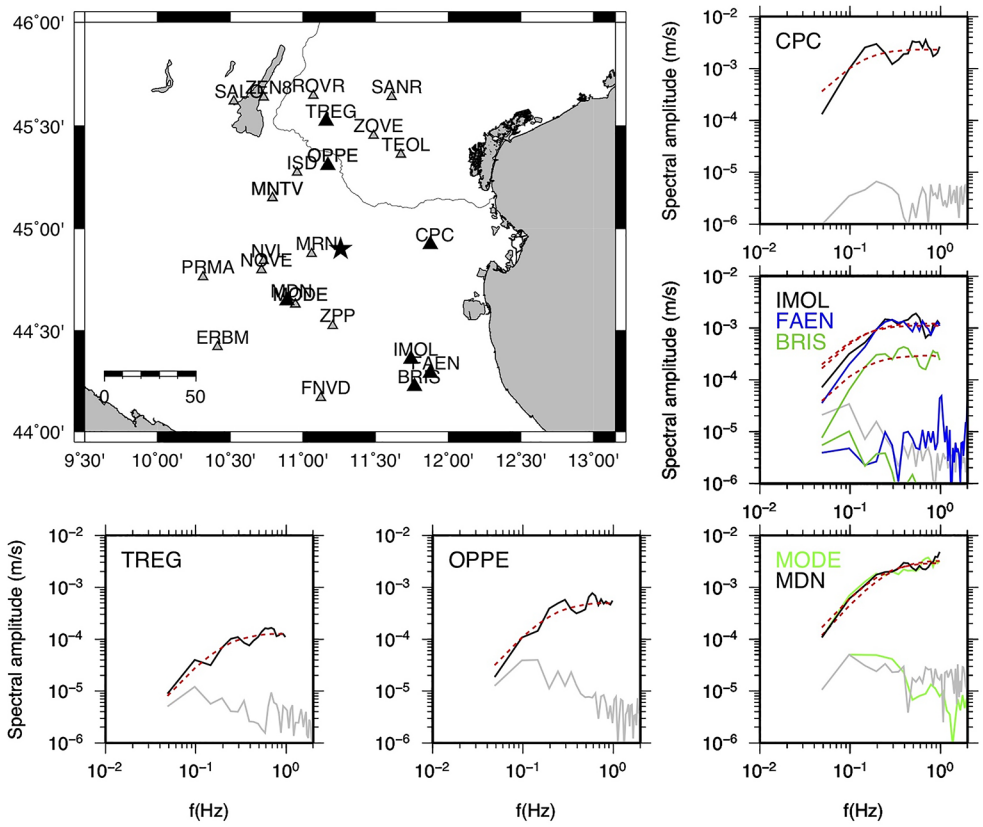

Figure 8. Map showing the location of the stations available for the spectral fitting (gray triangles) and those used to infer the best parameters (black triangles). The star identifies the epicenter of the May 20, M_L 5.9 (M_W 5.8). The side panels show the observed acceleration spectra (black line, green line, and blue line) at the stations indicated in the panel, the best fit spectra (red dashed line), and the pre-P spectrum of the noise (gray line, green line, and blue line).

to half of the available energy spent to create new fracture, indicating a fault not too hard to break. Thus, rather than the effect of fault strength we suggest that the low rupture velocity for the two main shocks in the sequence might be controlled by geometrical complexity. Indeed, it has been suggested that both events occurred on listric faults—with significant dip change with depth—embedded in the Ferrara arc, a complex geological and structural framework (e.g., Causse et al., 2017; Tondi et al, 2019).

The analysis of the static stress drop deduced from the slip distribution identifies the area of maximum slip as an asperity and suggests that the rupture stopped at a final stress level close to the kinematic friction level.

As for the role of the seismic source characteristics to the observed damage distribution, we observe that the detected damage pattern (Tertulliani, et al., 2012) exhibits two main lobes of higher damage in correspondence of the two dominant rupture directions inferred in our study. We conclude that the notably low rupture velocity contributed significant energy at low frequencies. This reflected in recorded peak ground velocities higher than predicted by the ground motion predictive equations (Barnaba et al., 2014), differently from peak ground acceleration in line with the expected values. Higher energy at low frequency could also explain the serious damage for industrial plants, which have natural period greater than that of ordinary buildings (Mucciarelli & Liberatore, 2014).

Table 1
List of the Stations Used for the Spectral Fitting

Station code	Lat(°)	Lon(°)	Elev.(m)	EC8 code	Network
BRIS	44.225	11.767	260	A*	INGV
CPC	44.921	11.876	2	C*	DPC
FAEN	44.290	11.877	41	C	INGV
IMOL	44.360	11.743	27	C	INGV
MODE	44.630	10.949	41	C*	INGV
MDN	44.646	10.889	37	C	DPC
OPPE	45.308	11.172	20	C*	INGV
TREG	45.523	11.161	342	C*	DPC

Notes: The Table contains the Station code, Stations coordinates, EC8 Site classification (Comité Europèen de Normalisation, 2004), based on Versus30—as reported by Castro et al. (2004)—and the managing institution. INGV refers to Istituto Nazionale di Geofisica e Vulcanologia, while DPC refers to Dipartimento della Protezione Civile Nazionale.

Data Availability Statement

Focal mechanisms are available at http://cnt.rm.ingv.it/. Waveforms have been downloaded from http://www.orfeus-eu.org/data/eida/. Figures were generated with Generic Mapping Tools (GMT; Wessel & Smith, 1991).

Acknowledgments
The authors thank the Associated Editor, Dr. Françoise Courboulex and an anonymous reviewer for their comments and suggestions that helped to improve the manuscript. The present study has been supported by Pianeta Dinamico-Working Earth INGV Project.

References

Anderson, J. G., & Hough, S. E. (1984). A model for the shape of the Fourier amplitude spectrum of acceleration at high frequencies. *Bulletin of the Seismological Society of America*, *71*, 1969–1993.

Andrews, D. J. (1980). A stochastic fault model, 1. Static case. *Journal of Geophysical Research: Solid Earth*, *85*(B7), 3867–3877. https://doi.org/10.1029/JB085iB07p03867

Akaike, H. (1974). A new look at the statistical model identification. *IEEE Transactions on Automatic Control*, *19*, 716–723. https://doi.org/10.1109/TAC.1974.1100705

Archuleta, R. J., & Hartzell, S. H. (1981). Effects of fault finiteness on near-source ground motion. *Bulletin of the Seismological Society of America*, *71*, 939–957.

Barnaba, C., Laurenzano, G., Moratto, L., Sugan, M., Vuan, A., Priolo, E., et al. (2014). Strong-motion observations from the OGS temporary seismic network during the 2012 Emilia sequence in northern Italy. *Bulletin of Earthquake Engineering*, *12*, 2165–2178. https://doi.org/10.1007/s10518-014-9610-4

Ben-Menahem, A. (1961). Radiation of seismic surface waves from finite moving sources. *Bulletin of the Seismological Society of America*, *51*(3), 401–435.

Bignami, C., et al. (2012). Coseismic deformation pattern of the Emilia 2012 seismic sequence imaged by Radarsat-1 interferometry. *Annals of Geophysics*, *55*, 4. https://doi.org/10.4401/ag-6157

Boatwright, J., & Fletcher, J. B. (1984). The partition of radiated energy between P and S waves. *Bulletin of the Seismological Society of America*, *74*, 361–376.

Bonini, L., Toscani, G., & Seno, S. (2014). Three-dimensional segmentation and different rupture behavior during the 2012 Emilia seismic sequence (Northern Italy). *Tectonophysics*, *630*, 33–42. http://dx.doi.org/10.1016/j.tecto.2014.05.006

Brune, J. N. (1970). Tectonic stress and the spectra of seismic shear waves from earthquakes. *Journal of Geophysical Research*, *75*, 4997–5009.

Castro, R. R., Pacor, F., Bindi, D., Franceschina, G., & Luzi, L. (2004). Site response of strong motion stations in the Umbria, central Italy, region. *Bulletin of the Seismological Society of America*, *71*, 576–590. https://doi.org/10.1785/0120030114

Castro, R. R., Pacor, F., Puglia, R., Ameri, G., Letort, J., Massa, M., & Luzi, L. (2013). The 2012 May 20 and 29, Emilia earthquakes (Northern Italy) and the main aftershocks: S-wave attenuation, acceleration source functions and site effects. *Geophysical Journal International*, *195*(1), 597–611. https://doi.org/10.1093/gji/ggt245

Causse, M., Cultrera, G., Moreau, L., Herrero, A., Schiappapietra, E., & Courboulex, F. (2017). Bayesian rupture imaging in a complex medium: The 29 May 2012 Emilia, Northern Italy, earthquake. *Geophysical Research Letters*, *44*, 7783–7792. https://doi.org/10.1002/2017GL074698

Cesca, S., Braun, T., Maccaferri, F., Passarelli, L., Rivalta, E., & Dahm, T. (2013). Source modelling of the M5–6 Emilia–Romagna, Italy, earthquakes (2012 May 20–29). *Geophysical Journal International*, *193*, 1658–1672. http://dx.doi.org/10.1093/gji/ggt069

Comité Européen de Normalisation (CEN) (2004). *Eurocode 8: Design of structures for earthquake resistance—Part 1: General rules, seismic actions and rules for buildings*. Brussels: Comité Européen de Normalisation.

Convertito, V., Catalli, F., & Emolo, A. (2013). Combining stress transfer and source directivity: the case of the 2012 Emilia seismic sequence. *Scientific Reports*, *3*, 3114. https://doi.org/10.1038/srep03114

Convertito, V., Pino, N. A., & Di Luccio, F. (2016). Investigating source directivity of moderate earthquakes by multiple approach: the 2013 Matese (southern Italy) $M_W = 5$ event. *Geophysical Journal International*, *207*, 1513–1528. https://doi.org/10.1093/gji/ggw360

Emolo, A., & Zollo, A. (2005). Kinematic source parameters for the 1989 Loma Prieta earthquake from the nonlinear inversion of accelerograms. *Bulletin of the Seismological Society of America*, *95*(3), 981–994. https://doi.org/10.1785/0120030193

Ganas, A., Roumelioti, Z., & Chousianitis, K. (2012). Static stress transfer from the May 20, 2012, M 6.1 Emilia-Romagna (northern Italy) earthquake using a co-seismic slip distribution model. *Annals of Geophysics*, *55*, 655–662. https://doi.org/10.4401/ag-61762012

Gelman, A., Carlin, B. J., Stern, H. S., & Rubin, D. B. (2004). *Bayesian data analysis*. Boca Raton, FL: Chapman & Hall/CRC. 978-1584883883.

Govoni, A., Marchetti, A., De Gori, P., Di Bona, M., Lucente, F. P., Improta, L., et al. (2014). The 2012 Emilia seismic sequence (Northern Italy): imaging the thrust fault system by accurate aftershock location. *Tectonophysics*, *622*, 44–55. https://doi.org/10.1016/j.tecto.2014.02.013

Graves, R. W., & Wald, D. J. (2001). Resolution analysis of finite fault source inversion using one- and three-dimensional Green's functions: 1. Strong motions. *Journal of Geophysical Research*, *106*, 8745–8766. https://doi.org/10.1029/2000JB900436

Guatteri, M., Mai, P. M., & Beroza, G. (2004). A pseudo-dynamic approximation to dynamic rupture models for strong ground motion prediction. *Bulletin of the Seismological Society of America*, *94*(6), 2051–2063. https://doi.org/10.1785/0120040037

Ide, S., & Beroza, G. C. (2001). Does apparent stress vary with earthquake size?. *Geophysical Research Letters*, *28*, 3349–3352. https://doi.org/10.1029/2001GL013106

Kanamori, H., Thio, H-K., Dreger, D., & Hauksson, E. (1992). Initial investigation of the Landers, California, earthquake of 28 June 1992 using TERRAscope. *Geophysical Research Letters*, *19*, 2267–2270. https://doi.org/10.1029/92GL02320

Király-Proag, E., Satriano, C., Bernard, P., & Wiemer, S. (2019). Rupture process of the Mw 3.3 earthquake in the St. Gallen 2013 geothermal reservoir, Switzerland. *Geophysical Research Letters*, *46*(14), 7990–7999. https://doi.org/10.1029/2019GL082911

Lai, C. G., Bozzoni, F., Mangriotis, M. D., & Martinelli, M. (2012). Geotechnical aspects of May 20, 2012 M5.9 Emilia earthquake, Italy. EUCENTRE Report V.1.0.

Lancieri, M., Madariaga, R., & Bonilla, F. (2012). Spectral scaling of the aftershocks of the Tocopilla 2007 earthquake in northern Chile. *Geophysical Journal International*, *189*, 469–480. https://doi.org/10.1111/j.1365-246X.2011.05327.x

Liberatore, L., Sorrentino, L., Liberatore, D., & Decanini, L. D. (2013). Failure of industrial structures induced by the Emilia (Italy) 2012 earthquakes. *Engineering Failure Analysis*, *34*, 629–647. https://doi.org/10.1016/j.engfailanal.2013.02.009

Liu, P., Custodio, S., & Archuleta, R. J. (2006). Kinematic inversion of the 2004 M 6.0 Parkfield earthquake including an approximation to site effects. *Bulletin of the Seismological Society of America*, *96*(4B), S143–S158. https://doi.org/10.1785/0120050826

Mai, P. M., & Beroza, G. C. (2002). A spatial random-field model for complex earthquake slip. *Journal of Geophysical Research*, *107*(B11). ESE 10-1-ESE 10-21. https://doi.org/10.1029/2001JB000588

Malagnini, L., Herrmann, R. B., Munafò, I., Buttinelli, M., Anselmi, M., Akinci, A., & Boschi, E. (2012). The 2012 Ferrara seismic sequence: Regional crustal structure, earthquake sources, and seismic hazard. *Geophysical Research Letters*, *39*, L19302. https://doi.org/10.1029/2012GL053214

Manfredi, G., Prota, A., Verderame, G. M., De Luca, F., & Ricci, P. (2013). Emilia earthquake, Italy: Reinforced Concrete building response. *Bulletin of Earthquake Engineering*, *12*(5), 2275–2298. https://doi.org/10.1007/s10518-013-9512-x

Masi, A., Santarsiero, G., Gallipoli, M. R., Mucciarelli, M., Manfredi, V., Dusi, A., & Stabile, T. A. (2013). Performance of the health facilities during the 2012 Emilia (Italy) earthquake and analysis of the Mirandola hospital case study. *Bulletin of Earthquake Engineering*, *12*(5), 2419–2443. https://doi.org/10.1007/s10518-013-9518-4

Metropolis, N., Rosenbluth, A. W., Rosenbluth, M. N., Teller, A. H., & Teller, E. (1953). Equation of state calculations by fast computing machines. *The Journal of Chemical Physics*, *21*, 1087–1092. https://doi.org/10.1063/1.1699114

Mori, J. J., Abercrombie, R. E., & Kanamori, H. (2003). Stress drops and radiated energies of the Northridge aftershocks. *Journal of Geophysical Research*, *108*(B11). ESE 13-1-ESE 13.12. https://doi.org/10.1029/200JB000474

Mucciarelli, M., & Liberatore, D. (2014). Guest editorial: The Emilia 2012 earthquakes. *Italy. Bull. Earthq. Eng.*, *12*, 2111–2116. https://doi.org/10.1007/s10518-014-9629-6

Pezzo, G., Merryman, J. P., Tolomei, C., Salvi, S., Atzori, S., Antonioli, A., et al. (2013). Coseismic deformation and source modeling of the May 2012 Emilia (Northern Italy) earthquakes. *Seismological Research Letters*, *84*(4), 645–655. http://dx.doi.org/10.1785/022012017

Piatanesi, A., Cirella, A., Spudich, P., & Cocco, M. (2007). A global search inversion for earthquake kinematic rupture history: Application to the 2000 western Tottori, Japan earthquake. *Journal of Geophysical Research*, *112*, B07314. https://doi.org/10.1029/2006JB004821

Piccinini, D., Pino, N. A., & Saccorotti, G. (2012). Source complexity of the May 20th, 2012, Mw=5.9 Ferrara (Italy) event. *Annals of Geophysics*, *55*, 569–573. http://doi.org/10.4401/ag-6111

Pino, N. A., Mazza, S., & Boschi, E. (1999). Rupture directivity of the major shocks in the 1997 Umbria-Marche (Central Italy) sequence from regional broadband waveforms. *Geophysical Research Letters*, *26*, 2101–2104. https://doi.org/10.1029/1999GL900464

Pino, N. A., Palombo, B., Ventura, G., Perniola, B., & Ferrari, G. (2008). Waveform modeling of historical seismograms of the 1930 Irpinia earthquake provides insight on 'blind' faulting in Southern Apennines (Italy). *Journal of Geophysical Research*, *113*, B05303. https://doi.org/10.1029/2007JB005211

Prieto, G. A., Thomson, D. J., Vernon, F. L., Shearer, P. M., & Parker, R. L. (2007). Confidence intervals for earthquake source parameters. *Geophysical Journal International*, *168*(3), 1227–1234. https://doi.org/10.1111/j.1365-246X.2006.03257.x

Rivera, L., & Kanamori, H. (2005). Representations of the radiated energy in earthquakes. *Geophysical Journal International*, *162*, 148–155. https://doi.org/10.1111/j.1365-246X.2005.02648.x

Scognamiglio, L., Tinti, E., & Quintiliani, M. (2006). *Time domain moment tensor* [Data set]. https://doi.org/10.13127/TDMT

Serpelloni, E., et al. (2012). GPS observations of coseismic deformation following the May 20 and 29, 2012, Emilia seismic events (northern Italy): Data, analysis and preliminary models. *Annals of Geophysics*, *55*, 4. https://doi.org/10.4401/ag-6168

Snoke, J. A. (1987). Stable determination of (Brune) stress drops. *Bulletin of the Seismological Society of America*, *77*, 530–538.

Somerville, P., et al. (1999). Characterizing crustal earthquake slip models for the prediction of strong ground motion. *Seismological Research Letters*, *70*(1), 59–80. https://doi.org/10.1785/gssrl.70.1.59

Stucchi, M., Meletti, C., Montaldo, V., Crowley, H., Calvi, G. M., & Boschi, E. (2011). Seismic hazard assessment (2003–2009) for the Italian building code. *Bulletin of the Seismological Society of America*, *101*, 1885–1911. https://doi.org/10.1785/0120100130

Tertulliani, A., Arcoraci, L., Berardi, M., Bernardini, F., Brizuela, B., Castellano, C., et al. (2012). The Emilia 2012 sequence: a macroseismic survey. *Annals of Geophysics*, *55*, 4. https://doi.org/10.4401/ag-6140

Tondi, R., Vuan, A., Borghi, A., & Argnani, A. (2019). Integrated crustal model beneath the Po Plain (Northern Italy) from surface wave tomography and Bouguer gravity data. *Tectonophysics*, *750*, 262–279. https://doi.org/10.1016/j.tecto.2018.10.018

Ventura, G., & Di Giovambattista, R. (2013). Fluid pressure, stress field and propagation style of coalescing thrusts from the analysis of the 20 May 2012 M_L 5.9 Emilia earthquake (northern Apennines, Italy). *Terra Nova*, *25*, 72–78. https://doi.org/10.1111/ter.12007

Wells, D. L., & Coppersmith, K. J. (1994). New empirical relationships among magnitude, rupture length, rupture width, rupture area, and surface displacement. *Bulletin of the Seismological Society of America*, *84*, 974–1002.

Wessel, P., & Smith, W. H. F. (1991). Free software helps map and display data. *Eos Transactions American Geophysical Union*, *72*, 441–446. https://doi.org/10.1029/90EO00319

Wyss, M. (1979). *Observation and interpretation of tectonic strain release mechanisms* (PhD thesis). California Institute of Technology, Pasadena.

Zollo, A., Orefice, A., & Convertito, V. (2014). Source parameter scaling and radiation efficiency of microearthquakes along the Irpinia fault zone in southern Apennines, Italy. *Journal of Geophysical Research*, *119*, 3256–3275. https://doi.org/10.1002/2013JB010116